Deciphering cooperative effects in plexciton formation between Ag nanocluster and fullerene

Tatsuya Yoshida,[1] Kazuya Watanabe,[1,*] Fumiharu Nishita,[1] Daiki Yamamoto,[1] Hiroshi Okuyama,[1,†] and Tomokazu Yasuike[2,‡]

[1]*Department of Chemistry, Graduate School of Science, Kyoto University, Kyoto 606-8502, Japan*

[2]*Division of Arts and Sciences, School of Graduate Studies, The Open University of Japan, Chiba 261-8586, Japan*

(Received 24 May 2023; revised 12 March 2024; accepted 12 April 2024; published 3 May 2024)

In this work, we use optical reflectance spectroscopy to study the plexciton formation between Ag nanoclusters and C_{60} molecules. The Ag clusters are fabricated on high-quality graphene under ultrahigh vacuum (UHV) and exhibit a strong absorption band at 3.4–3.6 eV due to the localized surface plasmons (LSPs). The plexciton formation is studied by depositing C_{60} on the Ag clusters in the same chamber under UHV. The deposition of C_{60} molecules leads to a splitting of the LSP band into multiple peaks with a systematic peak energy shift as a function of C_{60} coverage $\theta_{C_{60}}$. Notably, the details of the energy shifts and intensity variation sensitively depend on the LSP energy. Model calculations in which the plexciton coupling is approximated by a point-dipole interaction predict the evolution of the plexciton eigenenergy and oscillator strength with $\theta_{C_{60}}$ that reasonably explains the experiments. We demonstrate that spectral changes under the deposition of C_{60} cannot be explained by considering only one electronic transition in C_{60}, as is commonly assumed. Instead, it is necessary to take into account three electronic transitions of C_{60} and their intermixing with the LSP to fully comprehend the spectral evolution. The plexciton coupling energy is estimated to exceed 0.6 eV, indicating that the system reaches a strong coupling regime. Our findings suggest the importance of simultaneously considering multiple electronic excitations of molecules to understand strongly coupled plexcitons.

DOI: 10.1103/PhysRevB.109.195412

I. INTRODUCTION

The light-matter strong coupling (SC) between plasmon-polariton and quantum emitters (QEs) has attracted considerable interest in the last decades because it can serve as a promising platform for the next generation of quantum nanophotonics [1–5]. Although unavoidable large metallic loss occurs at the interface, plexcitons, a coupled mode between the plasmon-polariton and the excitons, have been detected and have gathered much attention. Notably, the extreme confinement of the electromagnetic field ensures a strong plasmon-exciton coupling with periodic array structures [6], propagating surface plasmons [7–10], Fabry-Pérot (FP) cavities [11–14], and localized surface plasmons (LSPs) [15–23].

While the recent progress toward single-particle observations [24–26] has revealed SC phenomena even in a single emitter limit [27,28], most of the works in the past utilized the cooperative effects to achieve SC: many QEs, an order of 1000 or more, are set to interact with a plasmon-polariton mode and the photon-exciton coupling is enhanced depending on the density of QE [9,21,25,29,30] as $\sqrt{N/V}$, where V is the volume of the cavity mode that contains N QEs [31]. Although several works in the past have studied the QE concentration dependence of the Rabi splitting [18,32], the nature of the collective coupling has not been elucidated well because neither the actual number of QEs interacting with a LSP mode nor the microscopic adsorption structure of QEs on metal nanoparticles (NPs) has been characterized well in those earlier works [33].

Here, we adopt a novel approach that sheds light on the problem by using surface science techniques: we prepare Ag NPs under an impurity-free condition in ultrahigh vacuum (UHV) and study the optical property of QEs (fullerene, C_{60}) adsorbed on the Ag NPs. A thermal deposition of Ag on high-quality graphene (Gr) monolayer leads to a formation of Ag clusters that exhibit a sharp LSP resonance at 3.4–3.6 eV reaching ∼70% absorption. The deposition of C_{60} on the Ag clusters leads to a multiple splitting of the LSP band due to the plexciton formation. Combined with temperature-programmed desorption (TPD) measurements of C_{60}, the evolution of the light-matter coupling as a function of the C_{60} coverage is elucidated. We further develop a novel theoretical method to explain the observed spectral evolution.

In this study, we demonstrate that it is not appropriate to treat quantum emitters (QEs) as two-level systems, as commonly assumed in many studies. This is because actual molecules inherently possess multiple excited states, and the approximation of treating them as two-level systems becomes inadequate when the plexciton eigenenergy becomes close to other excited states. The involvement of multiple excited states can lead to complexities in the plexciton absorption bands, which can obscure the conventional criteria of strong coupling, including Rabi splitting larger than the linewidth and anticrossing behavior with energy tuning. We suggest that

*kw@kuchem.kyoto-u.ac.jp
†hokuyama@kuchem.kyoto-u.ac.jp
‡yasuike@ouj.ac.jp

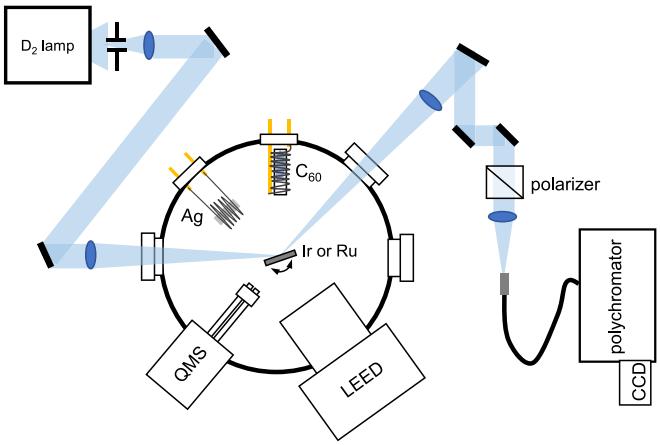

FIG. 1. A schematic illustration of the UHV chamber and the optical setup used in the experiment. QMS: quadrupole mass spectrometer.

quantum mixing of the electronic states through plexciton formation can occur even if these conventional criteria are not clearly observed. It is important to study the evolution of the plexciton absorption band with increasing QE density in a controlled manner and analyze the band shape using a reliable theoretical model.

Numerous approaches have been proposed to describe plexciton formations ranging from classical [34] and semiclassical treatments [35–37] to fully quantum mechanical ones [2,38,39]. For exploring the application of plexciton formation to the control of chemical reactions based on the hybridization of potential surfaces, a microscopic semiclassical or full quantum approach is required. Since the fully quantum, first-principles approaches [38,39] become intractable for large systems, the practically possible choice is a semiclassical one, in which the coupling strength between LSP and QE is evaluated as the innerproduct of the local electric field $\vec{E}_{\rm loc}$ and the transition dipole $\vec{\mu}$ of QE as $-\vec{E}_{\rm loc}\cdot\vec{\mu}$. In this work, we note that one can estimate a plasmonic field $\vec{E}_{\rm loc}$ from its transition dipole $\vec{\mu}_{\rm LSP}$, and that a plexciton system can be treated as a composite of many interacting transition dipoles. Such a treatment is equivalent to Kasha's exciton model [40] which has been used for the optical response of molecular aggregates and is then regarded as a minimal quantum approach that enables to include multiple excited states in QEs within a reasonable computational cost.

We study the hybridization between Ag LSP and three molecular excitations in C_{60} (from $1\,^1A_g$ to 1, 2, $3\,^1T_{1u}$) based on the Tavis-Cummings model [41,42] in which the excitonic coupling with Kasha's model is incorporated. Combined with realistic parameters obtained by the time-dependent density functional theory (TDDFT), the model successfully explains the observed evolution of the multiple splitting with increasing N.

II. METHODS

Figure 1 shows a schematic illustration of the experimental setup for the optical measurements. Experiments were carried out with an ultrahigh vacuum chamber with a base pressure of $<4\times10^{-8}$ Pa whose details have been described before [43–45]. Two kinds of substrates, Ir(111) and Ru(0001) (MaTecK, 99.99%), were used to support high-quality graphene sheets. The surfaces of the metal substrates were polished to be optically flat. An Ir(111) single crystal was cleaned by cycles of Ar^+ sputtering followed by annealing at 1470 K, showing a sharp (1×1) low-energy electron diffraction (LEED) pattern. Monolayer Gr on the Ir(111) surface was prepared by decomposition of ethylene in temperature-programmed growth followed by chemical vapor deposition [46,47]. Similar procedures were used for preparing a Gr on the Ru(0001) substrate. The quality and uniformity of Gr were confirmed by Moiré superstructure in LEED [Fig. 4(a)] [43]. Ag atoms were deposited from a hand-made evaporator in which a Ag wire is attached to a tungsten filament. The Ag deposition rate was estimated to be 0.2–0.6 nm/min and the sample temperature during the deposition was ∼298 K unless otherwise stated. C_{60} deposition onto the Ag-covered Gr was carried out by thermal evaporation of the C_{60} molecules (99.5%, purchased from Sigma-Aldrich and used without further purification) from an effusion cell made of quartz that is heated by an attached W wire.

We also carried out a separate scanning tunneling microscopy (STM) experiment at 78 K for the observation of Ag clusters on Gr/Ir(111) [48]. The Gr on Ir(111) was prepared in a similar way as described above, and the Ag atoms were evaporated from a silver wire wrapped around a tungsten wire placed 2 cm away from the surface. After the deposition at 300 K, the sample was immediately transferred to the STM at 78 K for observation. In another experiment, the sample was kept at 78 K during the deposition by using a different evaporator. The deposition rate was 3×10^{-2} and 4×10^{-3} ML/min at 300 and 78 K, respectively, where 1 ML corresponds to the surface atomic density of Ir(111).

The optical reflectivity change upon deposition of Ag or C_{60} was measured with white light from a deuterium lamp that was focused on the Ir or Ru crystal in the chamber. The reflected light was detected by a charge-coupled device camera attached to a polychromator. The measurement was carried out *in situ* during the deposition of the Ag atoms or C_{60} molecules at ∼298 K. The polarization of the detected light was chosen by a linear polarizer.

III. RESULTS AND DISCUSSION

A. Optical response of Ag on Gr

Figure 2(a) shows reflectivity change from the Ir(111) substrate as a function of the Ag deposition amount. While the reflectivity increases uniformly at 2.0–3.7 eV with the Ag amount, a sharp decrease is observed at higher than 3.7 eV due to the onset of the transitions from the d-band of Ag. These features are well reproduced by numerical simulations of the reflectivity of Ir substrate covered with a uniform Ag film obtained by a transfer-matrix method [Fig. 2(b), see Appendix A for the calculation details]. This means that the Ag deposition on a clean Ir(111) surface at room temperature leads to a smooth and uniform Ag film. The nominal thickness of the Ag film in the experiment is estimated by comparing

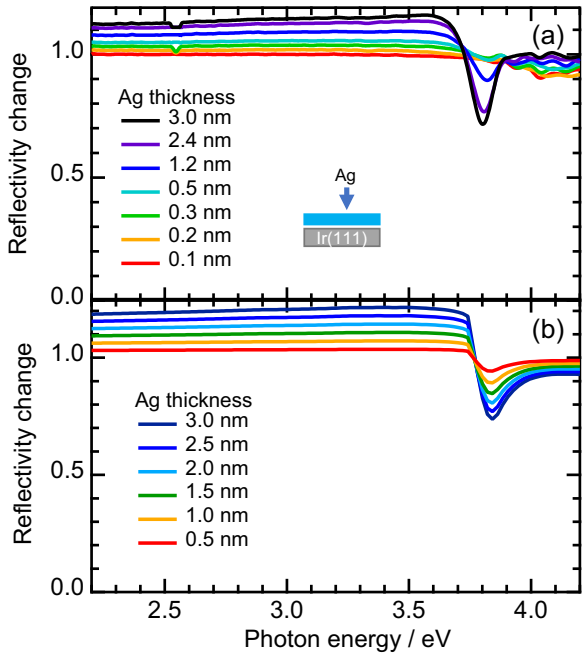

FIG. 2. (a) Reflectivity change $R(\theta_{Ag})/R(0)$ from Ir(111) (without graphene) as a function of the Ag nominal thickness θ_{Ag}. θ_{Ag} is indicated in the figure. $R(0)$ is defined as a reflectivity of the clean Ir(111) surface. The spectra were recorded for *p*-polarization light and the sample temperature was at room temperature. (b) Calculated reflectivity change $R(\theta_{Ag})/R(0)$ of Ir surface by using the transfer-matrix method described in Appendix A.

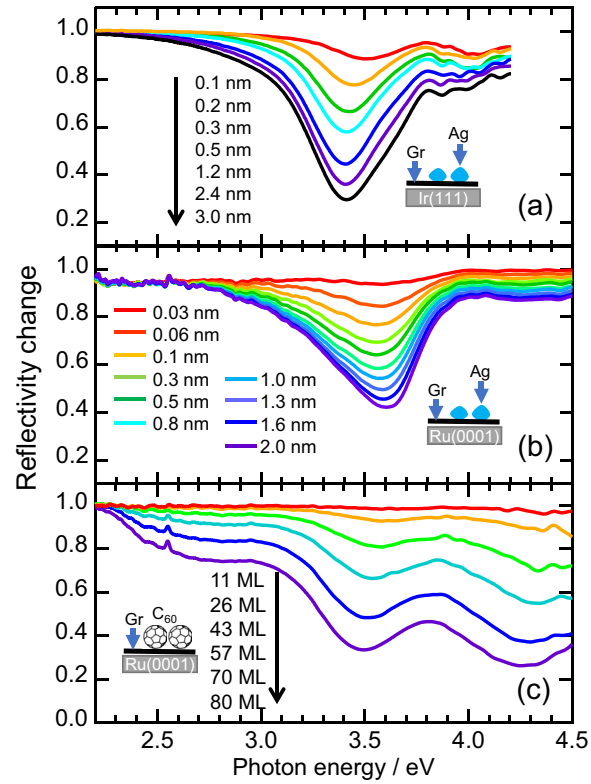

FIG. 3. $R(\theta_{Ag})/R(0)$ from Gr-covered (a) Ir(111) and (b) Ru(0001) as a function of Ag deposition amount. The estimated Ag coverages θ_{Ag} are indicated in the figure. (c) Reflectivity change $R(\theta_{C_{60}})/R(0)$ from the Ru(0001) covered with Gr as a function of the C_{60} coverage $\theta_{C_{60}}$ indicated in the figure (no Ag deposition). $R(0)$ stands for the reflectivity of Gr-covered Ir(111) for (a), and Gr-covered Ru(0001) for (b) and (c). The insets in (a)–(c) illustrate schematic adsorption behaviors for each condition. All the spectra were recorded for *p*-polarization light and the sample temperature was at room temperature.

the experimental reflectivity with those obtained by the simulation.

In contrast, the Ag deposition on Gr-covered substrates results in a strong reflectivity dip at 3.4–3.6 eV [Figs. 3(a) and 3(b)] whose magnitude grows with the deposition amount. The observed resonance energy at 3.4–3.6 eV is consistent with the previously reported LSP resonances of Ag nanoclusters [49–52]. Therefore it is conceivable that Ag clusters are formed on Gr by the deposition at room temperature.

The actual formation of the Ag clusters has been confirmed by the STM observation (see below, Sec. III C). Because the cluster size is less than 20 nm and those are formed on the optically flat Gr, an effect of the light scattering can be neglected in the observed response. Therefore hereafter we assume that the reflectivity decrease corresponds to the absorption by the clusters. This point is important for confirming SC because the splitting must be observed in the absorption spectra [53]. We also carried out numerical simulations that estimate the contribution of scattering by using Mie scattering theory [54]. In Appendix B, it is shown that the scattering cross section from a Ag 20 nm sphere is only a few percent of the absorption. This also supports the above assumption.

We propose that the strong absorption of the Ag clusters is due to an electronic decoupling from the substrate Ir (or Ru) by the presence of Gr, just like what has been observed recently for a thin layer of alkali atoms on Gr [43,55].

We note that the resonance energy varies by ∼0.1 eV depending on subtle differences in the preparation conditions (see Appendix C for different sets of data). Because Ag clustering occurs at step sites of Gr (see below, Sec. III C), this fluctuation may stem from that the local defect density at the steps depends on the details in the preparation procedure that is beyond control under the current setup. This brings sample-to-sample variations in the cluster size distributions causing the LSP energy variations. Despite the sample-to-sample small fluctuations in the resonance peak energy, the peak position of the LSP on the Gr-covered Ru(0001) tends to appear higher than that on the Gr-covered Ir(111) by 0.1–0.2 eV. The origin of the substrate dependence is not clear at this stage but may be derived from the difference in the Gr-metal interaction strength between these substrates [56] that would affect mean cluster size or the aspect ratios of the clusters. We demonstrate that the small difference in the LSP-resonance energy between the two substrates leads to a qualitative difference in the plexciton eigenstate evolution with the amount of coadsorbed C_{60} (see below).

B. LEED observation

Figures 4(a) and 4(b) show a LEED image of the sample (a) before and (b) after deposition of Ag with nominal coverage

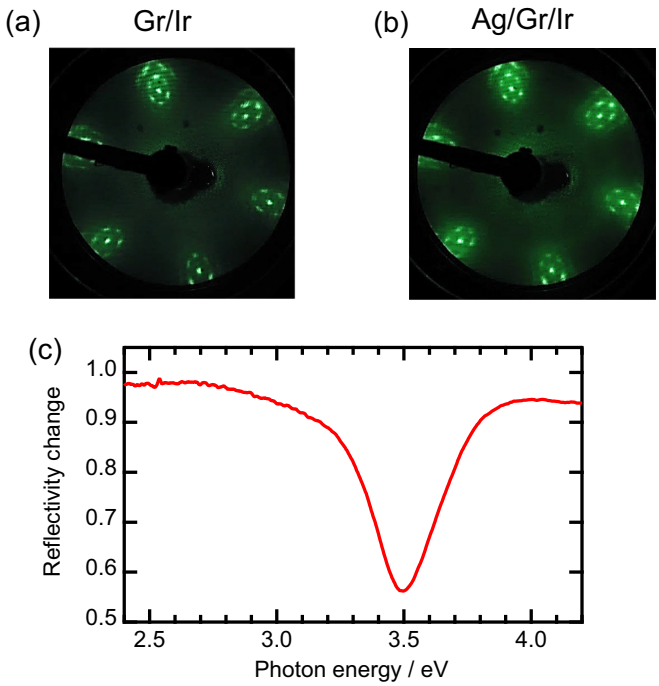

FIG. 4. LEED images of (a) Gr/Ir(111) and (b) Ag/Gr/Ir(111). LEED observations were carried out at 105 K and the beam energy was 83 eV. The Ag deposition was carried out at the room temperature. (c) A reflectivity change spectrum induced by the Ag deposition on the Gr/Ir(111) corresponding to the Ag coverage that gives the LEED image (b).

of ∼0.5 nm onto the Gr-covered Ir(111), respectively. We note that the Moiré pattern is preserved even with the deposition of a substantial amount of Ag indicating that the Ag clustering occurs at the wrinkles and steps of Gr leaving the terrace site undecorated as will be discussed in the following subsection.

The arrangements of metal nanoclusters on Gr by utilizing the Moiré superstructure as a template have been demonstrated for many substances including Pt [57,58], Ir [59], Rh [60], Ni [61], W; Re [62], and Ru [63]. However, the previous theoretical works have predicted that such a periodic cluster formation is not feasible for Ag because of its weak interaction with Gr that leads to a super diffusion of the atoms and clusters on Gr [64,65]. The results presented in this work are in line with these theoretical predictions.

C. STM observation

The clustering of Ag is characterized in real space by STM measurements. Figure 5(a) shows a large-scale image of Gr/Ir(111) that shows wrinkles of the Gr sheet and step structures of Gr reflecting the substrate Ir steps. The inset is an atomic-resolution image of Gr that shows a periodic Moiré structure [46,47]. Figure 5(b) shows an image of Gr/Ir(111) after Ag was deposited at 300 K. Most of the Ag clusters are located at the Gr steps, which is consistent with the previous observation that Ag clusters preferentially nucleate at defective sites on graphite [66,67].

The Ag clusters are not stable against the scanning of the STM tip: this is evidenced by the white wiggling curves that

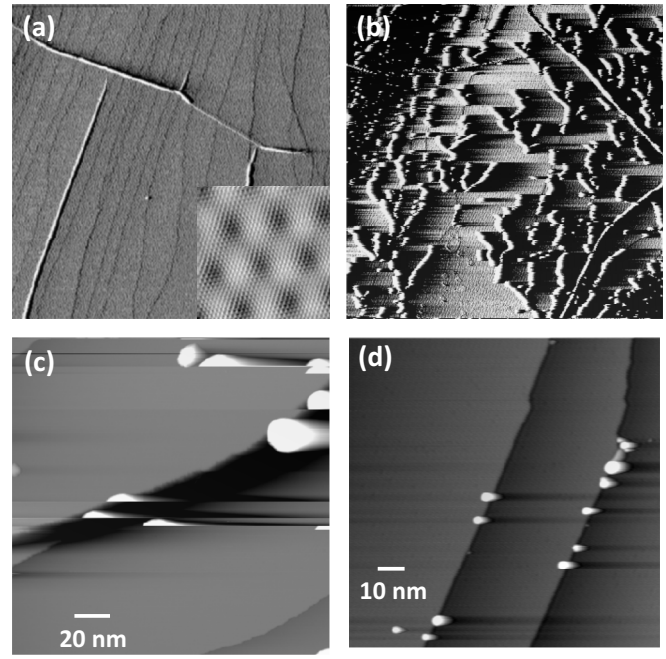

FIG. 5. (a) Large-scale STM image of Gr/Ir(111) recorded with sample voltage $V = -0.1$ V and tunneling current $I = 0.1$ nA. The inset shows the atomic image of Gr/Ir(111) that shows a periodic Moiré structure ($V = 0.03$ V and $I = 5$ nA). (b) The image after the deposition of Ag at 300 K ($V = -1.0$ V and $I = 0.03$ nA). (c) The image of Ag clusters formed at 300 K ($V = -1.5$ V and $I = 0.02$ nA). Most of the clusters appear to be fractional, indicating that they are displaced during the scanning of the tip over them. (d) The image of Ag clusters formed at 78 K ($V = -1.0$ V and $I = 0.03$ nA). All images were recorded at 78 K. The images (a) and (b) are shown by the derivative of tunnel current (dI/dx), where x is the scan direction (from left to right). The image size is 735 nm×735 nm for (a) and (b), and 7.3 nm×7.3 nm for the inset of (a).

show the traces of the dragged clusters [Fig. 5(b)]. While the instability of the clusters hampered the statistical analysis of their size, the upper limit of the cluster size at the step is estimated to be ∼20 nm [Fig. 5(c)]. The cluster nucleation at the step was also observed when the surface was kept at 78 K during the deposition [Fig. 5(d)], indicating that Ag atoms are mobile on the Gr/Ir(111) even at low temperatures.

D. C_{60} deposition on the Ag clusters

Before discussing the plexciton formation, the electronic spectra of C_{60} film on Gr is investigated. Figure 3(c) shows reflectivity change of C_{60} deposited on the Gr-covered Ru(0001) (without Ag clusters). A similar spectral shape was observed for C_{60} deposition on the Gr-covered Ir(111) (see Appendix D). Prominent dips (hence, absorption) appear at 2.7, 3.5–3.6, and 4.3–4.4 eV: Those are consistent with the earlier works on the spectra of a C_{60} film [68]. In the energy region of $E < 5.0$ eV, C_{60} is known to possess three dipole-allowed transitions at 3.04, 3.78, and 4.84 eV in *n*-hexane solution that have been ascribed to $1^1A_g \rightarrow 1^1T_{1u}$, $1^1A_g \rightarrow 2^1T_{1u}$, and $1^1A_g \rightarrow 3^1T_{1u}$ transitions, respectively [69]. The absorption spectra of the C_{60} film retain the

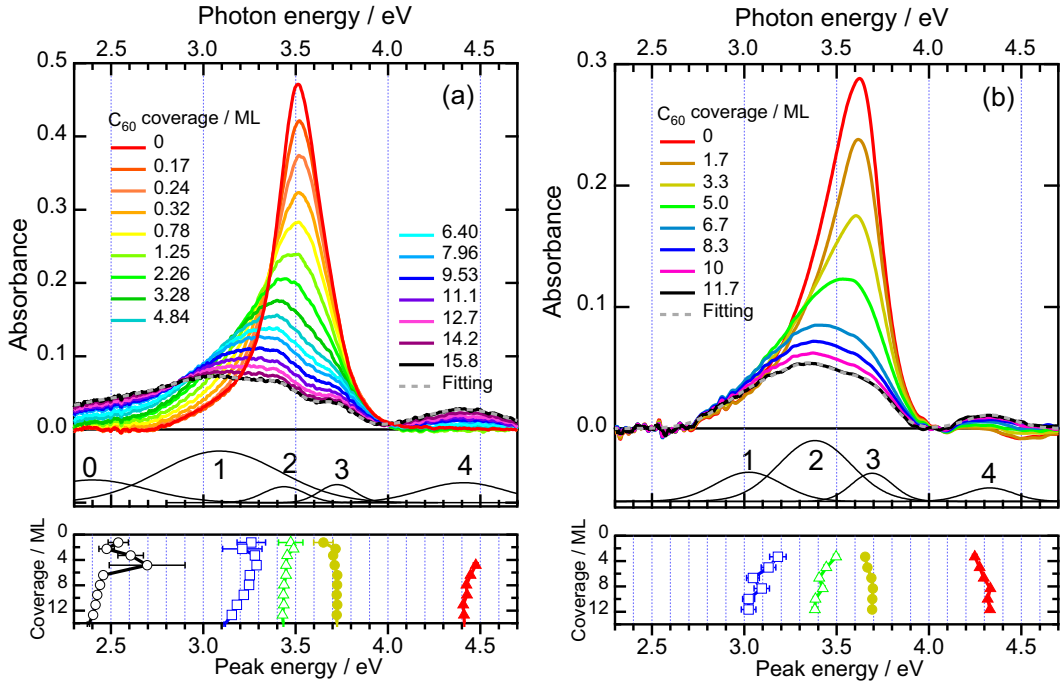

FIG. 6. Change of the absorption spectrum of Ag LSP induced by C_{60} deposition on (a) Gr/Ir(111) and (b) Gr/Ru(0001). The absorbance is defined by $-\log_{10}R(\theta_{Ag}, \theta_{C_{60}})/R(0, 0)$, where $R(\theta_{Ag}, \theta_{C_{60}})$ stands for a reflectivity of Gr with the deposition of Ag with a nominal thickness of θ_{Ag} and the subsequent deposition of C_{60} with the coverage of $\theta_{C_{60}}$. $\theta_{Ag} \approx 2.5$ nm in (a) and ≈2 nm in (b). $\theta_{C_{60}}$ are indicated in the figure. The middle panels show Gaussian components derived by fitting the curve for (a) $\theta_{C_{60}} = 15.8$ and (b) 11.7 ML. The labels 0 to 4 (1 to 4 for (b)) correspond to those in Figs. 9 and 10. A summation of the components is overlaid with a dashed-gray curve in the upper panels. See Appendix F for the background subtraction. Bottom panels for (a) and (b) show changes in the peak energy of the five (four) Gaussian components estimated by fitting the absorption spectra in Fig. 6(a) [Fig. 6(b)] as a function of C_{60} coverage. Open circles, open squares, open triangles, filled circles, and filled triangles correspond to the Gaussian components labeled 0–4, respectively.

characteristics of C_{60} in solution. Whereas the relatively intense absorption at 3.5–3.6 and 4.3–4.4 eV can be attributed to transitions to 2^1T_{1u} and 3^1T_{1u} states, respectively, the 2.7 eV peak observed in the film cannot be assigned to the transition to 1^1T_{1u}, because the predicted oscillator strength of the transition is too weak to account for the observed 2.7 eV peak intensity. Instead, the peak is considered to be an intermolecular transition (Wannier excitonic transition) rather than a local transition in C_{60} [70]. The transition to $2\,^1T_{1u}$ state at 3.5–3.6 eV is close to the Ag LSP resonance. Therefore the couplings between the Ag LSP and the C_{60} local transitions are naturally expected.

Having established the characterization of the Ag cluster formation on the Gr-covered substrates, and absorption spectrum of the C_{60} film, we discuss the effect of the C_{60} deposition on the Ag clusters. Figures 6(a) and 6(b) show the change in the absorption spectrum of LSP upon deposition of C_{60} on the Ag clusters on Gr/Ir(111) and Gr/Ru(0001), respectively. The signal in Fig. 6 is defined by $-\log_{10}\{R(\theta_{Ag}, \theta_{C_{60}})/R(0, 0)\}$, where $R(\theta_{Ag}, \theta_{C_{60}})$ is the optical reflectivity of Gr with the deposition of Ag (nominal thickness of $\theta_{Ag} = 2.0 - 2.5$ nm) and the subsequent deposition of C_{60} with a coverage of $\theta_{C_{60}}$. Here, $\theta_{C_{60}} = 1$ ML is defined as that C_{60} monolayer is completed on Gr/Ir(111). The coverage of C_{60} on the Ag deposited Gr/Ir is estimated by the TPD measurements (see Appendix E for further details). $\theta_{C_{60}}$ for the Gr/Ru substrate was estimated by assuming the same reduction ratio of the Ag LSP band area with $\theta_{C_{60}}$ as on the Gr/Ir substrate.

With increasing $\theta_{C_{60}}$, the Ag LSP absorption decreases with a broadening of the linewidth. In addition, a peak at around 4.3–4.5 eV appears at the higher coverages [Figs. 6(a) and 6(b)]. We carried out spectral decomposition analysis by assuming multiple Gaussian peaks and found that five (four) Gaussian components are sufficient to fit the signal for $\theta_{C_{60}} >$ 1 ML on Gr/Ir (Gr/Ru). An example of the decomposition is depicted in the middle panels in Fig. 6, showing a multiple peak splitting. Hereafter, those peaks are labeled as 0–4 (1–4 for Ru substrate) as indicated in the figures. The multiple splitting cannot be explained by the classical mean-field treatment that has been employed to explain the effect of thin oxide layers on LSP resonances [71–73]. Instead, it requires the quantum treatment that explicitly considers electronic excitations of C_{60}.

Variation of the peak energy as a function of $\theta_{C_{60}}$ is plotted in Fig. 6 bottom panels in which peaks 1 and 2 show a redshift but peak 3 shows a blue shift with $\theta_{C_{60}}$ for both substrates. Although the overall spectral evolution observed for the two substrates are similar, there are definite differences between them: The spectra for the Gr-covered Ir substrate exhibit much more pronounced redshift from the original LSP band as compared to the Gr-covered Ru substrate; the relative intensities of the multiple components are significantly different between the two substrates.

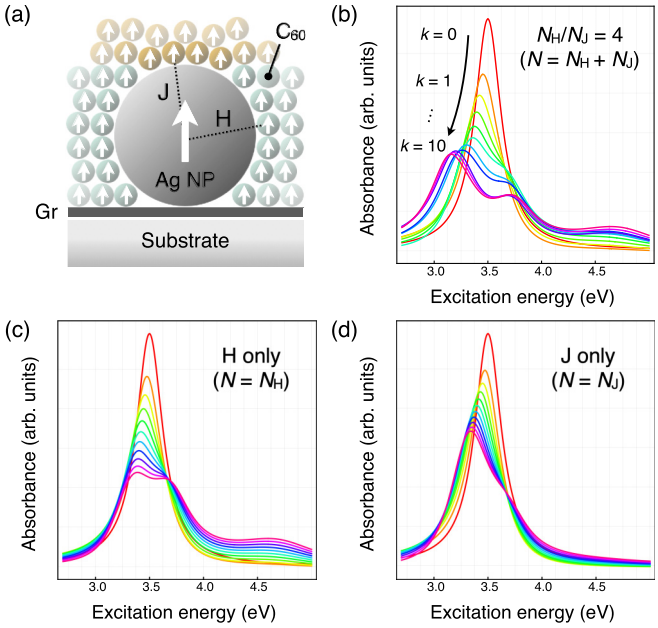

FIG. 7. (a) Schematic illustration of the model plexciton system assumed in this work. The surface normal components of the transition dipoles of Ag LSP and C_{60} molecules (white arrows) are considered and the couplings between them are approximated by Eq. (1). [(b)–(d)] Simulated absorption spectra of 20 nm Ag NP with (b) $N = N_H + N_J$ with $N_H/N_J = 4$ and $N^{max} = N_H^{max} + N_J^{max} = 2743$. The employed N values are $N = k\,(N^{max}/10)$, where k is an integer indicated in the figure; (c) all the couplings are assumed to be H-type: $N = N_H$ and $N_H^{max} = 2195$; and (d) all the couplings are assumed to be J-type $N = N_J$ and $N_J^{max} = 548$.

The observed spectral change with the C_{60} adsorption is not due to a simple superposition of the absorption band of C_{60} but to newly emergent bands by the plexciton formation. Because these spectral changes occur at multilayer region, $\theta_{C_{60}} > 1$ ML, the spectral change is not due to a permanent chemical change of Ag by interacting with C_{60}. We also note that the multilayer C_{60} is considered to form a close-packed film with a molecular density of ~ 1 nm^{-3}. It has been pointed out that for metal NPs decorated with QEs, QE number density of 1 nm^{-3} is required to obtain a clear SC signature on a typical Ag NP [74]. Although this has been noted to be difficult to achieve under conventional experiments [74], C_{60} deposition in the current study satisfies this criterion.

E. Tavis-Cummings-Kasha (TCK) model for describing plexciton formation

To understand the drastic changes in Ag NP spectra due to C_{60} deposition, we introduce a simplified theoretical model to consider a quantum-mechanical coupling among the Ag LSP and the three C_{60} excitations from $1\,^1A_g$ to $1, 2, 3\,^1T_{1u}$. In our excitonic approach for the plexciton formation, the light-matter coupling is simply expressed by the interaction between the transition dipoles of Ag LSP and C_{60} within the point-dipole approximation. As the major spectral evolution occurs at $\theta_{C_{60}} > 1$ ML, a direct overlap between Ag NP and C_{60} wave functions can be neglected justifying the approximation.

From the fact that the prominent Ag LSP is observed for p-polarization incident light, we consider the surface normal component of the transition dipoles both for the Ag LSP and the C_{60} excitations. A composite configuration depicted in Fig. 7(a) is assumed in which C_{60} molecules decorate the surface of the Ag cluster. The sign of the dipole coupling depends on the position of C_{60} molecules: the molecules on top of the cluster give rise to the J-type interaction in which the transition dipoles of the Ag LSP and C_{60} are aligned in a head-to-tail manner; those on the peripheral of the cluster give rise to the H-type interaction in which the transition dipoles are aligned in a parallel fashion. We note that these differences in the relative orientation of the transition dipoles lead to qualitative differences in the spectral intensity distribution of the newly formed plexciton states [see Figs. 7(c) and 7(d)]. In this work, we simplify the treatment by assuming that there are only two types of the relative orientation between the transition dipoles of C_{60} and the Ag LSP: J- and H-type in which the coupling energies are given by

$$W_{H,i} = \frac{\mu_{Ag}\mu_{C_{60},i}}{4\pi\epsilon_0 R^3} \quad \text{and} \quad W_{J,i} = -2W_{H,i}, \tag{1}$$

respectively, where R is the distance between Ag cluster and C_{60} that is given by the sum of radii of the Ag cluster and C_{60}; μ_{Ag} and $\mu_{C_{60},i}$ are magnitudes of transition dipoles for the Ag LSP and the C_{60} $1\,^1A_g \rightarrow i\,^1T_{1u}$ excitations ($i = 1, 2,$ and 3), respectively; ϵ_0 is the vacuum permittivity. This type of expression for the coupling matrix element was originally used to describe the optical excitations of molecular aggregates [40]. It is known to give a reasonable evaluation when the constituents are in van der Waals contact with each other [75].

The specific form of the Hamiltonian for the present system is

$$\hat{\mathcal{H}} = \begin{pmatrix} H_{Ag} & \sqrt{N_H}W_{H,1} & \sqrt{N_H}W_{H,2} & \sqrt{N_H}W_{H,3} & \sqrt{N_J}W_{J,1} & \sqrt{N_J}W_{J,2} & \sqrt{N_J}W_{J,3} \\ \sqrt{N_H}W_{H,1} & H_{C_{60},1} & 0 & 0 & 0 & 0 & 0 \\ \sqrt{N_H}W_{H,2} & 0 & H_{C_{60},2} & 0 & 0 & 0 & 0 \\ \sqrt{N_H}W_{H,3} & 0 & 0 & H_{C_{60},3} & 0 & 0 & 0 \\ \sqrt{N_J}W_{J,1} & 0 & 0 & 0 & H_{C_{60},1} & 0 & 0 \\ \sqrt{N_J}W_{J,2} & 0 & 0 & 0 & 0 & H_{C_{60},2} & 0 \\ \sqrt{N_J}W_{J,3} & 0 & 0 & 0 & 0 & 0 & H_{C_{60},3} \end{pmatrix}, \tag{2}$$

where N_H and N_J are the effective numbers of C_{60} in the H and J configurations.

The Hamiltonian of Eq. (2) is an extension of the Tavis-Cummings (TC) model [41,42] in which N identical two-level QEs interact with a single cavity mode. In the single-excitation subspace of the TC model, $N+1$ states couple to form two bright states and $N-1$ dark states. Since only these two bright states interact with each other, one can consider an effective Hamiltonian for the two bright states, and the coupling between the states in the effective Hamiltonian is $\sqrt{N}$ times the original cavity-emitter coupling [76]. The origin of the factor $\sqrt{N}$ is that the bright state created from N QEs is the permutation-invariant constructive superposition of N single QE excited configurations. In the present system, since we consider one Ag LSP and $3N_H + 3N_J$ C_{60} excitations, the dimension of the original TC Hamiltonian is the $3N_H + 3N_J + 1$ and is reduced to 3+3+1=7 in the corresponding bright-state effective Hamiltonian. Since the single cavity-emitter coupling in Eq. (2) is given as the Kasha's excitonic interaction, the model introduced above should be called the Tavis-Cumming-Kasha (TCK) model.

The diagonal elements of H_X are assumed to be complex numbers in order to express the finite linewidths of the excitations [77],

$$H_X = \hbar\omega_X - i\gamma_X, \tag{3}$$

where $\hbar\omega_X$ and γ_X are the diabatic excitation energy and half-width of the excitation X, respectively. The label X distinguishes the excitations: X = Ag and C_{60}, i (i = 1, 2, and 3) mean the Ag LSP and C_{60} $1\,^1A_g \rightarrow i\,^1T_{1u}$ ones, respectively.

The parameters required for constructing the effective Hamiltonian were determined as follows. For Ag NP, assuming Ag_n clusters generally have spherical structures, we modeled them as regular icosahedrons. This modeling corresponds to considering Ag_n with

$$n = 13,\ 55,\ 147, \ldots, \frac{(2m+1)(5m^2+5m+3)}{3}, \tag{4}$$

where m is a positive integer. We roughly assumed that the oscillator strengths f_n and cluster volumes V_n are proportional to n. The used expressions are given by

$$f_n = 0.13462n, \quad V_n = 185.81n\ a_0^3, \tag{5}$$

where a_0 is the Bohr radius. These relations were determined by the TDDFT calculation of Ag_{13} based on the screened range-separated hybrid functional with the polarizable continuum model (SRSH-PCM) [70,78] with the basis sets of def2-SVPD [79–81]. For mimicking the dielectric environment of graphene, the dielectric constant was set to be 3.05. We can estimate the radii and the LSP transition dipoles of general Ag clusters μ_{Ag} from Eq. (5). As described later, the excitation energy was treated as a variable parameter in the vicinity of the experimental value. The C_{60} parameters were estimated by the same SRSH-PCM TDDFT method with the basis set of 6-31+G* [82–84]. The computed transition energies/oscillator strengths are 3.46 eV/0.047, 3.80 eV/0.34, and 4.83 eV/1.36, respectively. In the following simulations, these excitation energies were shifted 0.2 eV lower so that the excitation to 2^1T_{1u} is consistent with the experimentally observed 3.6 eV (see Appendix D for the details). All the half-linewidths γ_X were set to the present experimental values ($\gamma_{Ag} = 0.15$ eV, $\gamma_{C_{60},1} = \gamma_{C_{60},2} = 0.25$ eV, $\gamma_{C_{60},3} = 0.5$ eV).

The optical spectrum $\sigma(E)$ is computed by the standard procedure based on the expression of

$$\sigma(E) = -\frac{1}{\pi}\mathrm{Im}\langle\Psi_0\hat{\mu}|\frac{1}{E-\hat{\mathcal{H}}}|\hat{\mu}\Psi_0\rangle, \tag{6}$$

where E, Ψ_0, and $\hat{\mu}$ are the excitation energy, the wave function of the ground state for the whole system, and the transition dipole operator, respectively. Figure 7(b) shows the simulation results using parameters that give a prediction close to the experimental results for the Ir substrate [Fig. 6(a)]. This result is obtained by assuming 20 nm Ag NP (Ag_{221481}) for N ($\equiv N_H + N_J$) values from 0 to $N_H^{max} + N_J^{max}$. Here we assume $N_H/N_J = 4$ and set $N_H^{max} = 2195$ and $N_J^{max} = 548$.

We note that the spectral shape strongly depends on the H-, J-character of the couplings. Figures 7(c) and 7(d) show simulation results as in Fig. 7(b) but with $N = N_H$ and $N_H^{max} = 2195$ in (c) and $N = N_J$ and $N_J^{max} = 548$ in (d). Given that all the couplings are the H-type (c), the higher energy peaks gain prominent intensity. In contrast, under the dominance of the J-type coupling (d), the lowest energy peak becomes prominent, and the 4.7 eV peak disappears. The experimental feature may lie in between these two extremes and it is reasonable that the appropriate ratio found in our survey, $N_H/N_J = 4$, roughly corresponds to the area ratio of the sides to the top of a sphere put on a plane. We further note that the coupling through LSP cooperatively intermixes the spatially separated H- and J-type interactions leading to a larger peak splitting than that attained solely by either of the H- or J-type interactions.

F. Spectral evolution with increasing number of QE by plexciton formation

Figures 8(a)–8(d) show a series of simulation results on the Ag LSP-C_{60} plexciton formation with the TCK model. We examine how the tuning of the LSP resonance energy across the transition of C_{60} molecule affects the N dependence of the plexciton eigenenergy. From Figs. 8(a) to 8(d), the Ag LSP energy is varied from 3.4 to 3.7 eV. Because the second C_{60} electronic transitions is set to be 3.6 eV, the Ag LSP energy is tuned across the C_{60} $1\,^1A_g \rightarrow 2\,^1T_{1u}$ excitation energy from Figs. 8(a) to 8(d).

The spectral evolution exhibits the following features: diagonalizing the effective Hamiltonian Eq. (2) brings 7 eigenstates. In the limit of $N \rightarrow 0$, these are categorized as three degenerate pair states corresponding to the three C_{60} transitions and as the Ag LSP. With increasing N, the C_{60} transitions start to mix with the Ag LSP and shift in their energy. The bottom traces of Figs. 8(a)–8(d) show the evolution of the eigenenergies of the seven eigenstates as a function of N. We note that the H-J mixing brings a state capable of coupling with the Ag LSP by constructive interference of the two couplings (LSP-bright state) and also brings a state incapable of coupling with the Ag LSP caused by destructive interference of them (LSP-dark state). Therefore the degeneracy in the three C_{60} transitions at $N \rightarrow 0$ is lifted with increasing N, and each state is split into two: one is the LSP-bright state that shows energy shift with increasing N and the other is

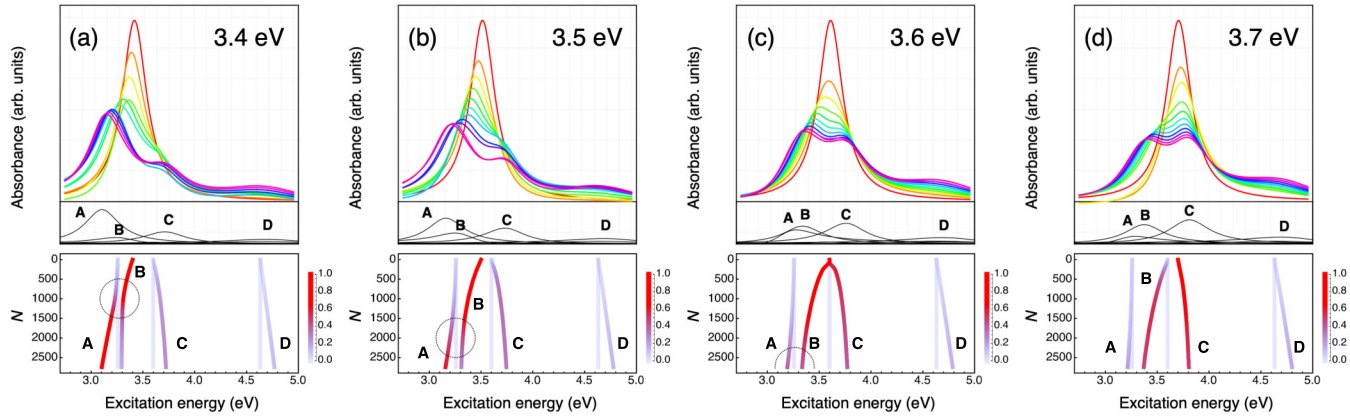

FIG. 8. (Top) The absorption spectra for Ag NP–$(C_{60})_N$ composite systems calculated from Eq. (6). The Ag LSP excitation energy is set to be (a) 3.4, (b) 3.5, (c) 3.6, and (d) 3.7 eV. The employed $N = N_H + N_J$ Values and color codes are the same as in Fig. 7(b). (Middle) Absorption spectra of the LSP-bright states A–D at $N = N_{max}$. (Bottom) Eigenenergy shift of the eigenstate with N. The color code of the plot indicates the fraction of Ag LSP in each eigenstate. Because the LSP oscillator strength is much larger than that of monomer C_{60}, the actual absorption strength of the plexciton state is determined by the LSP fraction contained in the eigenstate. The pale straight lines indicate the energy of the LSP-dark states (see Appendix G). At the upper edge ($N \to 0$), each eigenstate corresponds to the four diabatic states: Ag LSP; i^1T_{1u} excitations ($i = 1, 2,$ and 3). Circles in (a)–(c) indicate the region of the avoided crossing between the LSP-bright states A and B.

the LSP-dark state whose energy is insensitive to N (see Appendix G for the mathematical background of the emergence of the LSP-dark states). We note that the original Ag LSP oscillator strength is much larger than those of three C_{60} transitions and hence the absorption strength of the plexciton state is determined by the fraction of Ag LSP contained in each eigenstate that is indicated by color code in the bottom traces in Figs. 8(a)–8(d). The three straight lines with pale color in each bottom trace of Figs. 8(a)–8(d) correspond to the LSP-dark state with no fraction of Ag LSP and hence coincide with the three C_{60} electronic transition energies (3.26 eV, 3.60 eV, and 4.63 eV). As is indicated by the color code of the bottom traces, the oscillator strength is mainly carried by the four LSP-bright states that exhibit systematic energy shift with N. These four excitations are labeled as A to D in order of the excitation energy in Fig. 8. The middle traces in Figs. 8(a)–8(d) show spectrum of each component A–D for $N = 2743$.

The Ag LSP is primarily mixed with the C_{60} $2\,^1T_{1u}$ state at small N values, but the feature of the intensity transfer is highly sensitive to the detuning between the Ag LSP energy and the C_{60} $2\,^1T_{1u}$ transition at 3.6 eV. In Fig. 8(a), assuming the lowest LSP energy of 3.4 eV, the resultant plexciton states repel as N increases. The lower-energy state shows a downward shift and becomes close to the C_{60} $1\,^1T_{1u}$ state. Then, these two states exhibit an avoided crossing at around $N = 1000$ [the circle in the bottom panel in Fig. 8(a)], and the oscillator strength is transferred to the lower plexciton state.

While the features observed at higher Ag LSP energy can be explained similarly, the point of the avoided crossing shifts to a larger N value with increasing Ag LSP energy [the circles in the bottom panels in Figs. 8(b) and 8(c)], and the avoided feature becomes obscured. Concomitantly, the transfer of the oscillator strength shifts to the higher-energy eigenstates.

The predicted spectral evolution of the plexciton with N captures the key features of the experiment (Fig. 6), including (i) the reduction of the LSP absorption upon adsorption of C_{60}; (ii) splitting in the multiple peaks that show systematic energy shift with increasing N. The spectral changes observed in the experiment do not exhibit the behavior of the commonly assumed two-state TC model, but they agree well with the present TCK model based on a microscopic Ag NP-C_{60} geometric configuration. It should be noted that the peaks in the experimental spectra for large $\theta_{C_{60}}$ are broader than the simulated ones. This broadening may be ascribed to inhomogenious distributions in the cluster morphology and in the C_{60} position-dependent coupling strength, neglected in the current simulations.

The subtle differences recognized between the two substrates, Ir and Ru, can be rationalized by considering the difference in the Ag LSP resonance energy between these substrates: from the experimental Ag LSP energy, Fig. 8(b) is close to the case of the Gr-covered Ir substrate ($\hbar\omega_{Ag} = 3.5$ eV) and (c) is to the case of the Gr-covered Ru substrate ($\hbar\omega_{Ag} = 3.6$ eV). Figure 9 (Fig. 10) shows the evolution of the energy and height of the simulated peaks A–C in Fig. 8 compared with those of the Gaussian components labeled 1–3 obtained from the spectral decompositions of the experimental data in Fig. 6(a) [Fig. 6(b)].

The simulation demonstrates significant characteristics that were observed in the experiments. For $\hbar\omega_{Ag} = 3.5$ eV, which corresponds to the case of the Gr-covered Ir substrate, eigenstates A and B show avoided crossing at $N \simeq 1800$ concomitant with the intensity transfer from the latter to the former [Figs. 9(a) and 9(c)]. The corresponding avoided crossing between the components 1 and 2 occurs in the experiment at around 4 ML [Fig. 9(b)], which is evidenced by the intensity transfer between these two components at the same C_{60} coverage in Fig. 9(d).

For the slightly higher $\hbar\omega_{Ag}$ at 3.6 eV, which corresponds to the case of the Gr-covered Ru substrate, the eigenstates C and B are degenerate at $N \to 0$ and strongly intermix showing increasing energy splitting with N [Fig. 10(a)]. The upshift of the LSP energy to 3.6 eV leads to a separation in

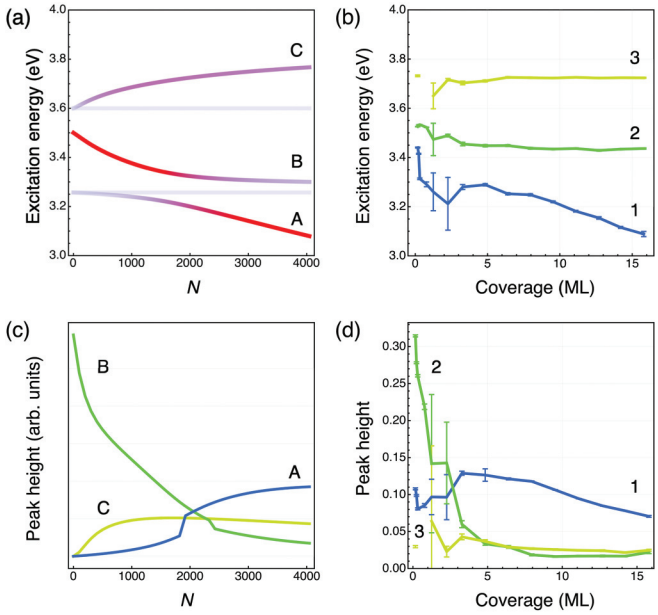

FIG. 9. (a) N dependence of the eigenenergy of the lowest three LSP-bright states for $\hbar\omega_{\mathrm{Ag}} = 3.5$ eV [same data depicted in Fig. 8(b)]. The color code of the plot indicates the fraction of the Ag LSP state in each plexciton eigenstate. (b) C_{60} coverage dependence of the peak energy of the components 1–3 of the plexciton experimentally observed for the Ir substrate [Fig. 6(a)]. (c) N dependence of the peak height of the each LSP-bright state in (a) for $\hbar\omega_{\mathrm{Ag}} = 3.5$ eV. The label in the figure corresponds to those in Fig. 8(b). (d) C_{60} coverage dependence of the height of the Gaussian components 1–3 in Fig. 6(a).

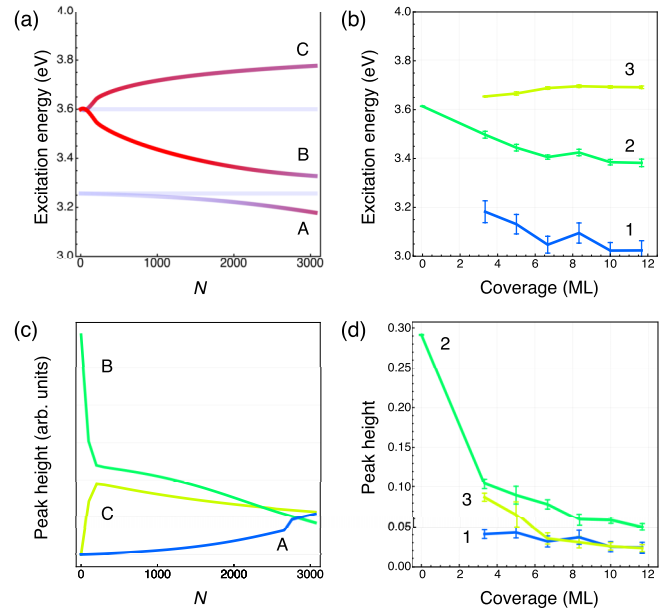

FIG. 10. (a) N dependence of the eigenenergy of the lowest three LSP-bright states for $\hbar\omega_{\mathrm{Ag}} = 3.6$ eV [same data depicted in Fig. 8(c)]. The color code of the plot indicates the fraction of the Ag LSP state in each plexciton eigenstate. (b) C_{60} coverage dependence of the peak energy of the components 1–3 of the plexciton experimentally observed for the Ru substrate [Fig. 6(b)]. (c) N dependence of the peak height of the each LSP-bright state in (a) for $\hbar\omega_{\mathrm{Ag}} = 3.6$ eV. The label in the figure corresponds to those in Fig. 8(c). (d) C_{60} coverage dependence of the height of the Gaussian components 1–3 in Fig. 6(b).

eigenenergies between the states A and B [Fig. 10(a)], bringing the avoided crossing point between A and B to larger N than in the case for $\hbar\omega_{\mathrm{Ag}} = 3.5$ eV in Fig. 9(a). This suppresses the mixing between A and B leading to a much smaller intensity transfer to A state than in Fig. 9(a). This is reflected in the experiment in which peaks 2 and 3 repel from each other with $\theta_{C_{60}}$ [Fig. 10(b)] in line with the simulation and the energy of peak 1 varies in parallel with that of peak 2 without a feature of avoided crossing. Consequently, the height of peaks 1–3 monotonously decreases with $\theta_{C_{60}}$ [Fig. 10(d)]: no significant intensity transfer is observed in contrast to Fig. 9(d). Although the mixing between A and B occurs at around $N = 2800$ in the simulation [Fig. 10(a)], this is not clear in the experiment [Fig. 10(b)] probably due to the obscuring by the inhomogeneous broadening. In this way, the subtle difference in the spectral evolution between the two substrates can be rationalized as the difference in the N dependence of the plexciton eigenenergy caused by the slight variation in the Ag LSP resonance energy between the two substrates.

Because of the complexity in the energy structure of the plexciton states due to the involvement of the multiple electronic excitations, it is not straightforward to extract the light-matter coupling strength from the observed spectra in Fig. 6. Instead, the above analysis with the TCK model allows us to decipher the intermixing of the Ag LSP and C_{60} excitations, and if we regard the peak separation between peaks 1 and 3 that reaches about 0.6 eV at $\theta_{C_{60}} = 15$ ML as the effective coupling strength, one can conclude that a strong coupling is attained in the Ag-C_{60} composite.

Here we comment on the origin of the lowest-energy component found in Gr-covered Ir substrate [peak 0 in Fig. 6(a)]. We consider that this component is derived from the mixing between the Ag LSP and the excitonic transition in C_{60} film found at 2.7 eV [Fig. 2(c)]. Because the transition is not incorporated in the current simulations, the corresponding component is absent in Fig. 8. The reason why we do not see the corresponding component in Fig. 6(b) may be that much less intensity transfer occurs to the lowest state because of the slightly higher LSP energy for the Gr-covered Ru substrate than the other one.

IV. CONCLUSION

In conclusion, Ag deposition on a well-defined Gr brings about a cluster formation that exhibits a sharp LSP resonance band at 3.4–3.6 eV. The C_{60} adsorption on the Ag clusters leads to a significant intensity reduction and broadening of the peak. The TCK model incorporating an excitonic coupling scheme by using a point-dipole approximation reveals the underlying plexciton eigenenergy structure involving the multiple excited states of C_{60}. The analysis shows that the intensity reduction of the LSP band is a clear signature of the plexciton formation in which the oscillator strength of the LSP is transferred to the plexciton states. The coupling between Ag-C_{60} pairs in different geometric configurations

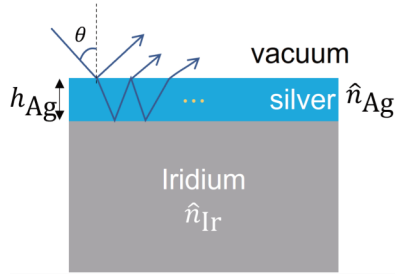

FIG. 11. Model structure assumed in the transfer matrix calculation.

leads to four bright states that exhibit systematic eigenenergy shift with N. It is notable that the evolution of the plexciton eigenenergy with N sensitively depends on a small variation of the Ag-LSP transition energy, and this explains the experimentally observed substrate dependence of the spectral evolution with the C_{60} adsorption.

The success of the current theoretical approach demonstrates that it is not sufficient to consider only the QE excitation at near resonance to the LSP. Instead, the multiple optically allowed excitations of QE must be taken into account to describe plexciton formation. While the focus has been paid to whether or not the spectral features predicted by the two-state TC model are observed, the model should be considered applicable only when the polariton eigenstates are far apart from other electronic transitions.

We emphasize that the plexciton formation involving multiple excited-states of QE can lead to a drastic modification of the potential energy landscape in the excited states [76,85]. A significant practical advantage of the plexciton in the surface co-adsorption systems is their tunability: the mixing ratio of the LSP and the molecular excitations can be flexibly adjusted by changing the amount of adsorption. This tunability paves the way for increasing the degree of freedom in the plexcitonic control of molecular reactions. In addition, the fact that the plexciton eigenenergy structure is sensitive to the fine-tuning between the LSP and QE transition energies also provides a useful parameter for modifying the electronic structure of the hybrid states.

ACKNOWLEDGMENTS

This work is supported by the Grants-in-Aid for Scientific Research (B) (No. JP21H01886) and the Grant-in-Aid for Challenging Research (Pioneering) (No. JP21K18202) from the Japan Society for the Promotion of Sciences (JSPS KAKENHI); JST CREST Grant No. JPMJCR20R4, Japan. We thank N. Nagatsuka and T. Koitaya for their assistance.

APPENDIX A: REFLECTIVTY PREDICTION BY A TRANSFER MATRIX METHOD

Reflectivity change of Ir substrate upon deposition of the Ag thin film is predicted by using a transfer matrix method (characteristic matrix method) with assuming the ideal multilayer structure depicted in Fig. 11. We define the tangential components of the electric field and magnetic field of the incident light with vacuum wavelength λ at the interface i ($i = 1, 2$) as E_i and H_i. For p-polarized light incident on the sample with an angle of θ,

$$\begin{pmatrix} E_1 \\ H_1 \end{pmatrix} = \begin{pmatrix} \cos\delta & i\sin\delta/Y \\ i\sin\delta \cdot Y & \cos\delta \end{pmatrix} \begin{pmatrix} E_2 \\ H_2 \end{pmatrix} \equiv \begin{pmatrix} m_{11} & m_{12} \\ m_{21} & m_{22} \end{pmatrix} \begin{pmatrix} E_2 \\ H_2 \end{pmatrix}, \tag{A1}$$

where $Y = \sqrt{\epsilon_0/\mu_0} \cdot (\hat{n}_{Ag}/\cos\theta_{Ag})$; $\delta = (2\pi/\lambda)\hat{n}_{Ag} h_{Ag} \cos\theta_{Ag}$. By using complex reflactive index of Ag $\hat{n}_{Ag}$ and Ir $\hat{n}_{Ir}$, the complex angle θ_{Ag} and θ_{Ir} are defined as $\sin\theta = \hat{n}_{Ag}\sin\theta_{Ag} = \hat{n}_{Ir}\sin\theta_{Ir}$.

The reflection amplitude r is given by

$$r = \frac{Y_0(m_{11} + Y_{Ir}m_{12}) - (m_{21} + Y_{Ir}m_{22})}{Y_0(m_{11} + Y_{Ir}m_{12}) + (m_{21} + Y_{Ir}m_{22})}, \tag{A2}$$

where $Y_0 = \sqrt{\epsilon_0/\mu_0}/\cos\theta$; $Y_{Ir} = \sqrt{\epsilon_0/\mu_0} \cdot (\hat{n}_{Ir}/\cos\theta_{Ir})$.

The reflectivity change, $R(\theta_{Ag})/R(0)$, is simulated by calculating $|r|^2/|r_0|^2$, where r_0 is the reflection amplitude of Ir substrate. The optical constants of Ag and Ir are taken from the literature [86]. Calculation results for several Ag thicknesses are shown in Fig. 2(b).

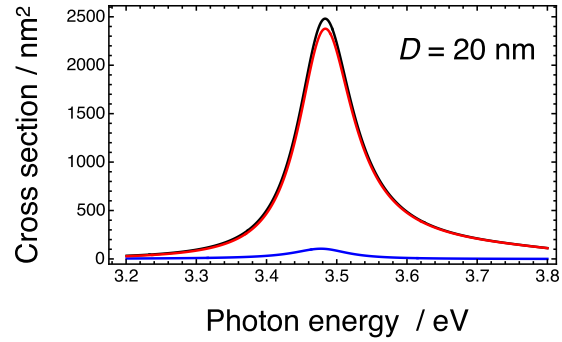

FIG. 12. Absorption (red) and scattering (blue) cross-section of a Ag nanosphere with 20 nm diameter obtained from Mie scattering theory. The black curve is a sum of the other two components.

APPENDIX B: ESTIMATION OF A SCATTERING CROSS-SECTION OF AG NANOSPHERE

Figure 12 shows numerical Mie-scattering simulations of scattering and absorption cross-sections for a 20 nm Ag sphere in the vacuum. The optical constant of Ag is taken from the literature [86].

APPENDIX C: REPRODUCIBILITY OF THE OPTICAL SPECTRUM

Figure 13 shows other sets of data for the absorption spectra of Ag clusters deposited on Gr and subsequent spectral change induced by C_{60} deposition on it. Although the preparation procedure was the same for the two sets of data as described in the main text, the peak energy of the Ag LSP shows small fluctuations. We note that the overall spectral change induced by the plexciton formation with C_{60} deposition is reasonably reproduced. The small discrepancy between the plexciton spectra (black and blue solid curves) may reflect

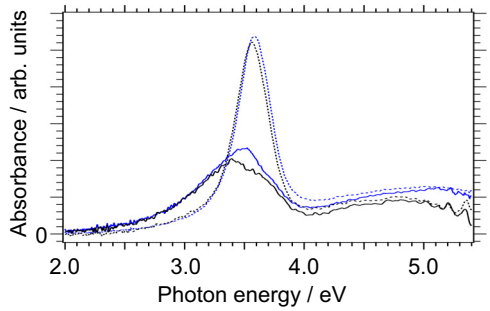

FIG. 13. Absorption spectrum of the Ag clusters on Gr/Ir(111) (Dashed curves) and Ag clusters with C_{60} deposition (Solid curves, $\theta_{C_{60}} \sim 3$ ML). Black and blue colors indicate different sets of run with the same procedure.

the LSP peak energy dependence of the plexciton eigenenergy discussed in Sec. III F.

APPENDIX D: SUBSTRATE DEPENDENCE OF THE ABSORPTION SPECTRA OF C_{60} FILMS

Figure 14 shows reflectivity change upon deposition of C_{60} film on Gr for the two substrates (Ir(111) and Ru(0001)). The prominent peaks of the C_{60} $2\,^1T_{1u}$ transitions are observed at 3.6 eV for both substrates. The peak energy shows a redshift with increasing the coverage as is demonstrated in Fig. 3(c). Because the plexciton formation is examined for $\theta_{C_{60}} < 20$ ML in this work, we set the $2\,^1T_{1u}$ transition energy to be 3.6 eV in our simulations (Figs. 7 and 8).

APPENDIX E: TEMPERATURE-PROGRAMMED DESORPTION (TPD) OF C_{60}

Figure 15(a) show TPD traces of C_{60} ($m/e = 60$) from Gr/Ir(111) and from Ag deposited Gr/Ir(111). The peak at 720 K ($\theta_{C_{60}} = 0.3$ and 1.2 ML) are ascribed to the desorption of C_{60} directly adsorbs on the Ag clusters because they are absent on the trace from Gr/Ir(111) without Ag clusters [the dotted curve in Fig. 15(a)]. We note that here $\theta_{C_{60}} = 1$ ML is defined as a monolayer C_{60} coverage that fully covers the Gr/Ir(111) surface without Ag clusters. In addition to these components, a further increase in the C_{60} coverage [Fig. 15(a), 3.3 ML, the green curve] brings multiple peaks at 580, 500, and 470 K. As the peaks at the lowest two temperatures,

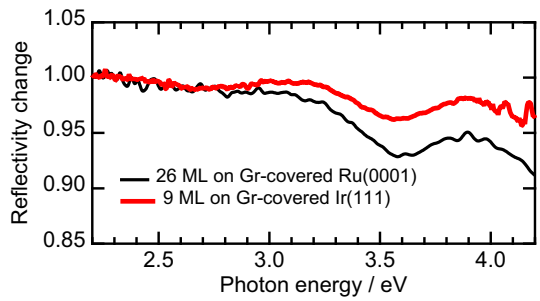

FIG. 14. Reflectivity change upon adsorption of C_{60} films on Gr supported by (red) Ir(111) and (black) Ru(0001). C_{60} coverage is indicated in the figure.

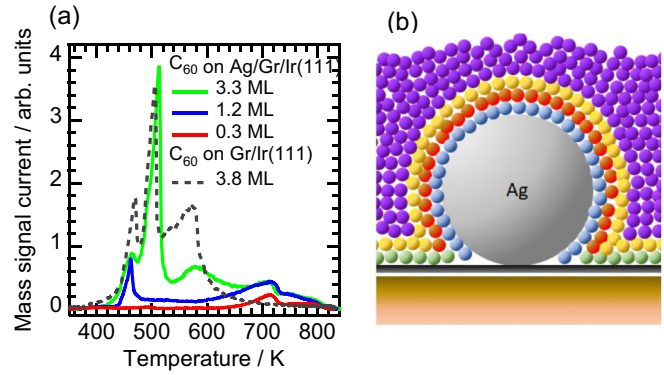

FIG. 15. (a) (solid curves) TPD traces ($m/e = 60$) of C_{60} adsorbed on the Ag deposited Gr/Ir(111). The coverage of C_{60} is indicated in the figure. (Dashed curve) TPD trance of C_{60} adsorbed on Gr/Ir(111) (without Ag). (b) A schematic illustration of C_{60} adsorption on the Ag cluster (side view). The large silver sphere is the Ag cluster. Smaller spheres are C_{60}. The color code of C_{60} indicates different desorption temperatures (hence, different adsorption binding energy, see text).

namely at 500 and 470 K, are observed also in the TPD trace of C_{60} from Gr/Ir(111), these are ascribed to the desorption from the second and the higher layers of C_{60}, respectively. The peak at 580 K in Fig. 15(a) (3.3 ML, green curve) is ascribed to a desorption of C_{60} interacting with other C_{60} directly adsorbing on Ag clusters. Further increase in $\theta_{C_{60}} > 3$ ML results in monotonous growth of the lowest temperature peak (470 K) showing a zeroth order desorption (not shown). Figure 15(b) shows a schematic illustration of the adsorption of C_{60} on a Ag cluster. The highest temperature desorption is assigned to the direct adsorption on the Ag cluster (the blue small spheres). The second-nearest adsorption on the cluster (the red small spheres) would give rise to the TPD component at around 600 K, whereas C_{60} directly adsorbs on Gr (the green small spheres) may desorb at a similar temperature. The next layer (indicated by yellow small spheres) desorbs at 510 K. Further increase in the coverage (the purple small spheres) gives rise to the multilayer desorption at around 470 K.

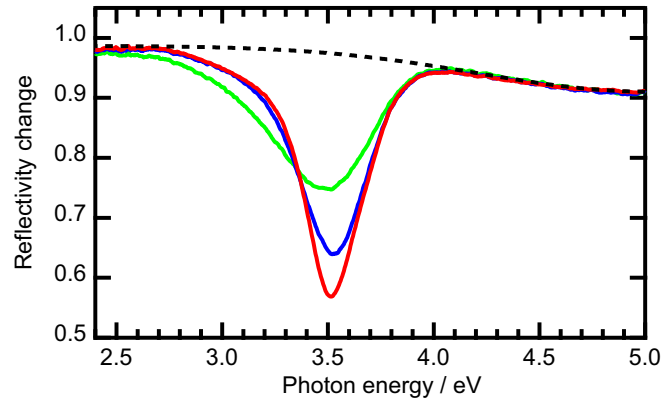

FIG. 16. (Solid curves) some of the original data of the reflectivity change depicted in Fig. 6. (Dashed curve) A Gaussian function obtained by fitting the background component of the spectra.

Therefore the adsorption nature of C_{60} molecules that bring the spectral shift depicted in Fig. 2 is mainly the multilayer (>1 ML) adsorption with cohesive energy close to that of bulk C_{60}.

APPENDIX F: BACKGROUND SUBTRACTION FROM THE REFLECTIVITY CHANGE SPECTRA

Figure 16 shows original data for the reflectivity change induced by the C_{60} deposition onto the Ag adsorbed Gr/Ir(111) shown in Fig. 6 in the main text. As the data exhibit some background components that do not depend on the C_{60} dosage, the background is subtracted by fitting with a Gaussian function (black dashed curve). The spectra shown in Fig. 6 have been subjected to this background subtraction procedure.

APPENDIX G: THE MATHEMATICAL ORIGINS OF THE LSP-DARK STATE

The mathematical background for the appearance of the LSP-dark states is explained as follows. For the assumed condition of $N_{\mathrm{H}}/N_{\mathrm{J}} = 4$, the Hamiltonian of Eq. (2) is reduced to the form of

$$\hat{\mathcal{H}} = \begin{pmatrix} H_{\mathrm{Ag}} & \tilde{W}_1 & \tilde{W}_2 & \tilde{W}_3 & -\tilde{W}_1 & -\tilde{W}_2 & -\tilde{W}_3 \\ \tilde{W}_1 & H_{\mathrm{C_{60},1}} & 0 & 0 & 0 & 0 & 0 \\ \tilde{W}_2 & 0 & H_{\mathrm{C_{60},2}} & 0 & 0 & 0 & 0 \\ \tilde{W}_3 & 0 & 0 & H_{\mathrm{C_{60},3}} & 0 & 0 & 0 \\ -\tilde{W}_1 & 0 & 0 & 0 & H_{\mathrm{C_{60},1}} & 0 & 0 \\ -\tilde{W}_2 & 0 & 0 & 0 & 0 & H_{\mathrm{C_{60},2}} & 0 \\ -\tilde{W}_3 & 0 & 0 & 0 & 0 & 0 & H_{\mathrm{C_{60},3}} \end{pmatrix}, \tag{G1}$$

where $\tilde{W}_i = \sqrt{N_{\mathrm{H}}} W_{\mathrm{H},i}$. It is easy to show that this matrix has the following three trivial eigenvectors regardless of the value of N_{H},

$$\boldsymbol{v}_1 = {}^{\mathrm{t}}(0, 1, 0, 0, 1, 0, 0), \tag{G2}$$

$$\boldsymbol{v}_2 = {}^{\mathrm{t}}(0, 0, 1, 0, 0, 1, 0), \tag{G3}$$

$$\boldsymbol{v}_3 = {}^{\mathrm{t}}(0, 0, 0, 1, 0, 0, 1), \tag{G4}$$

and it is also immediately apparent that the corresponding eigenvalues for $\boldsymbol{v}_i$ are $H_{\mathrm{C_{60},}i}$. This means that each eigenenergy of the three states is equal to the excitation energy of C_{60} without coupling to Ag LSP. Therefore the eigenenergy of the LSP-dark states is independent of N (Fig. 8 in the main text). These are the mathematical origins of the LSP dark states.

[1] N. T. Fofang, N. K. Grady, Z. Fan, A. O. Govorov, and N. J. Halas, Plexciton dynamics: Exciton–plasmon coupling in a J-aggregate–Au nanoshell complex provides a mechanism for nonlinearity, Nano Lett. **11**, 1556 (2011).

[2] A. Manjavacas, F. J. García de Abajo, and P. Nordlander, Quantum plexcitonics: Strongly interacting plasmons and excitons, Nano Lett. **11**, 2318 (2011).

[3] M. S. Tame, K. R. McEnery, S. K. Oezdemir, J. Lee, S. A. Maier, and M. S. Kim, Quantum plasmonics, Nat. Phys. **9**, 329 (2013).

[4] P. Törmä and W. L. Barnes, Strong coupling between surface plasmon polaritons and emitters: a review, Rep. Prog. Phys. **78**, 013901 (2015).

[5] A. P. Manuel, A. Kirkey, N. Mahdi, and K. Shankar, Plexcitonics – fundamental principles and optoelectronic applications, J. Mater. Chem. C **7**, 1821 (2019).

[6] A. I. Väkeväinen, R. J. Moerland, H. T. Rekola, A.-P. Eskelinen, J.-P. Martikainen, D.-H. Kim, and P. Törmä, Plasmonic surface lattice resonances at the strong coupling regime, Nano Lett. **14**, 1721 (2014).

[7] J. Bellessa, C. Bonnand, J. C. Plenet, and J. Mugnier, Strong coupling between surface plasmons and excitons in an organic semiconductor, Phys. Rev. Lett. **93**, 036404 (2004).

[8] J. Dintinger, S. Klein, F. Bustos, W. L. Barnes, and T. W. Ebbesen, Strong coupling between surface plasmon-polaritons and organic molecules in subwavelength hole arrays, Phys. Rev. B **71**, 035424 (2005).

[9] P. Vasa, W. Wang, R. Pomraenke, M. Lammers, M. Maiuri, C. Manzoni, G. Cerullo, and C. Lienau, Real-time observation of ultrafast Rabi oscillations between excitons and plasmons in metal nanostructures with J-aggregates, Nat. Photon. **7**, 128 (2013).

[10] S. Aberra Guebrou, C. Symonds, E. Homeyer, J. C. Plenet, Y. N. Gartstein, V. M. Agranovich, and J. Bellessa, Coherent emission from a disordered organic semiconductor induced by strong coupling with surface plasmons, Phys. Rev. Lett. **108**, 066401 (2012).

[11] T. Schwartz, J. A. Hutchison, C. Genet, and T. W. Ebbesen, Reversible switching of ultrastrong light-molecule coupling, Phys. Rev. Lett. **106**, 196405 (2011).

[12] D. Lidzey, D. Bradley, M. Skolnick, T. Virgili, S. Walker, and D. Whittaker, Strong exciton-photon coupling in an organic semiconductor microcavity, Nature (London) **395**, 53 (1998).

[13] J. R. Tischler, M. S. Bradley, V. Bulović, J. H. Song, and A. Nurmikko, Strong coupling in a microcavity led, Phys. Rev. Lett. **95**, 036401 (2005).

[14] S. Kena-Cohen and S. R. Forrest, Room-temperature polariton lasing in an organic single-crystal microcavity, Nat. Photon. **4**, 371 (2010).

[15] N. I. Cade, T. Ritman-Meer, and D. Richards, Strong coupling of localized plasmons and molecular excitons in nanostructured silver films, Phys. Rev. B **79**, 241404(R) (2009).
[16] Y. Sugawara, T. A. Kelf, J. J. Baumberg, M. E. Abdelsalam, and P. N. Bartlett, Strong coupling between localized plasmons and organic excitons in metal nanovoids, Phys. Rev. Lett. **97**, 266808 (2006).
[17] W. Ni, Z. Yang, H. Chen, L. Li, and J. Wang, Coupling between molecular and plasmonic resonances in freestanding dye-gold nanorod hybrid nanostructures, J. Am. Chem. Soc. **130**, 6692 (2008).
[18] N. T. Fofang, T.-H. Park, O. Neumann, N. A. Mirin, P. Nordlander, and N. J. Halas, Plexcitonic nanoparticles: Plasmon-exciton coupling in nanoshell-J-aggregate complexes, Nano Lett. **8**, 3481 (2008).
[19] S. Balci, Ultrastrong plasmon-exciton coupling in metal nanoprisms with J-aggregates, Opt. Lett. **38**, 4498 (2013).
[20] G. Zengin, G. Johansson, P. Johansson, T. J. Antosiewicz, M. Kall, and T. Shegai, Approaching the strong coupling limit in single plasmonic nanorods interacting with J-aggregates, Sci. Rep. **3**, 3074 (2013).
[21] A. E. Schlather, N. Large, A. S. Urban, P. Nordlander, and N. J. Halas, Near-field mediated plexcitonic coupling and giant Rabi splitting in individual metallic dimers, Nano Lett. **13**, 3281 (2013).
[22] M. Wersäll, J. Cuadra, T. J. Antosiewicz, S. Balci, and T. Shegai, Observation of mode splitting in photoluminescence of individual plasmonic nanoparticles strongly coupled to molecular excitons, Nano Lett. **17**, 551 (2017).
[23] S. Balci, B. Kucukoz, O. Balci, A. Karatay, C. Kocabas, and G. Yaglioglu, Tunable plexcitonic nanoparticles: A model system for studying plasmon–exciton interaction from the weak to the ultrastrong coupling regime, ACS Photon. **3**, 2010 (2016).
[24] A. Bek, R. Jansen, M. Ringler, S. Mayilo, T. A. Klar, and J. Feldmann, Fluorescence enhancement in hot spots of AFM-designed gold nanoparticle sandwiches, Nano Lett. **8**, 485 (2008).
[25] G. Zengin, M. Wersäll, S. Nilsson, T. J. Antosiewicz, M. Käll, and T. Shegai, Realizing strong light-matter interactions between single-nanoparticle plasmons and molecular excitons at ambient conditions, Phys. Rev. Lett. **114**, 157401 (2015).
[26] A. B. Yankovich, B. Munkhbat, D. G. Baranov, J. Cuadra, E. Olsén, H. Lourenço-Martins, L. H. G. Tizei, M. Kociak, E. Olsson, and T. Shegai, Visualizing spatial variations of plasmon-exciton polaritons at the nanoscale using electron microscopy, Nano Lett. **19**, 8171 (2019).
[27] K. Hennessy, A. Badolato, M. Winger, D. Gerace, M. Atatuere, S. Gulde, S. Faelt, E. L. Hu, and A. Imamoglu, Quantum nature of a strongly coupled single quantum dot-cavity system, Nature (London) **445**, 896 (2007).
[28] A. Faraon, I. Fushman, D. Englund, N. Stoltz, P. Petroff, and J. Vuckovic, Coherent generation of non-classical light on a chip via photon-induced tunnelling and blockade, Nat. Phys. **4**, 859 (2008).
[29] F. Todisco, M. De Giorgi, M. Esposito, L. De Marco, A. Zizzari, M. Bianco, L. Dominici, D. Ballarini, V. Arima, G. Gigli, and D. Sanvitto, Ultrastrong plasmon-exciton coupling by dynamic molecular aggregation, ACS Photon. **5**, 143 (2018).
[30] H. Wang, A. Toma, H.-Y. Wang, A. Bozzola, E. Miele, A. Haddadpour, G. Veronis, F. De Angelis, L. Wang, Q.-D. Chen, H.-L. Xu, H.-B. Sun, and R. P. Zaccaria, The role of Rabi splitting tuning in the dynamics of strongly coupled J-aggregates and surface plasmon polaritons in nanohole arrays, Nanoscale **8**, 13445 (2016).
[31] Y. Kaluzny, P. Goy, M. Gross, J. M. Raimond, and S. Haroche, Observation of self-induced Rabi oscillations in two-level atoms excited inside a resonant cavity: The ringing regime of superradiance, Phys. Rev. Lett. **51**, 1175 (1983).
[32] T. K. Hakala, J. J. Toppari, A. Kuzyk, M. Pettersson, H. Tikkanen, H. Kunttu, and P. Törmä, Vacuum Rabi splitting and strong-coupling dynamics for surface-plasmon polaritons and rhodamine 6G molecules, Phys. Rev. Lett. **103**, 053602 (2009).
[33] C. Tserkezis, A. I. Fernàndez-Domínguez, P. A. D. Gonçalves, F. Todisco, J. D. Cox, K. Busch, N. Stenger, S. I. Bozhevolnyi, N. A. Mortensen, and C. Wolff, On the applicability of quantum-optical concepts in strong-coupling nanophotonics, Rep. Prog. Phys. **83**, 082401 (2020).
[34] T. Ambjörnsson, G. Mukhopadhyay, S. P. Apell, and M. Käll, Resonant coupling between localized plasmons and anisotropic molecular coatings in ellipsoidal metal nanoparticles, Phys. Rev. B **73**, 085412 (2006).
[35] L. Novotny and B. Hecht, *Principles of Nano-Optics* (Cambridge University Press, Cambridge, 2012).
[36] N. A. Mortensen, Mesoscopic electrodynamics at metal surfaces – from quantum-corrected hydrodynamics to microscopic surface-response formalism, Nanophotonics **10**, 2563 (2021).
[37] F. Della Sala, R. Pachter, and M. Sukharev, Advances in modeling plasmonic systems, J. Chem. Phys. **157**, 190401 (2022).
[38] T. P. Rossi, T. Shegai, P. Erhart, and T. J. Antosiewicz, Strong plasmon-molecule coupling at the nanoscale revealed by first-principles modeling, Nat. Commun. **10**, 3336 (2019).
[39] K. Iida, M. Noda, K. Ishimura, and K. Nobusada, First-principles computational visualization of localized surface plasmon resonance in gold nanoclusters, J. Phys. Chem. A **118**, 11317 (2014).
[40] M. Kasha, H. R. Rawls, and M. A. El-Bayoumi, The exciton model in molecular spectroscopy, Pure Appl. Chem. **11**, 371 (1965).
[41] M. Tavis and F. W. Cummings, Exact solution for an *N*-molecule–radiation-field hamiltonian, Phys. Rev. **170**, 379 (1968).
[42] M. Tavis and F. W. Cummings, Approximate solutions for an *N*-molecule–radiation-field hamiltonian, Phys. Rev. **188**, 692 (1969).
[43] S. Tanaka, T. Yoshida, K. Watanabe, Y. Matsumoto, T. Yasuike, M. Petrović, and M. Kralj, Linewidth narrowing with ultimate confinement of an alkali multipole plasmon by modifying surface electronic wave functions with two-dimensional materials, Phys. Rev. Lett. **125**, 126802 (2020).
[44] K. Watanabe, Y. Matsumoto, T. Yasuike, and K. Nobusada, Adsorbate-localized versus substrate-mediated excitation mechanisms for generation of coherent Cs-Cu stretching vibration at Cu(111), J. Phys. Chem. A **115**, 9528 (2011).
[45] D. Ino, K. Watanabe, N. Takagi, and Y. Matsumoto, Electron transfer dynamics from organic adsorbate to a semiconductor surface: Zinc phthalocyanine on TiO_2(110), J. Phys. Chem. B **109**, 18018 (2005).
[46] R. van Gastel, A. T. N'Diaye, D. Wall, J. Coraux, C. Busse, N. M. Buckanie, F.-J. Meyer zu Heringdorf, M. Horn von Hoegen, T. Michely, and B. Poelsema, Selecting a single

orientation for millimeter sized graphene sheets, Appl. Phys. Lett. **95**, 121901 (2009).

[47] A. T. N'Diaye, J. Coraux, T. N. Plasa, C. Busse, and T. Michely, Structure of epitaxial graphene on Ir(111), New J. Phys. **10**, 043033 (2008).

[48] H. Okuyama, D. Yamamoto, S. Hatta, and T. Aruga, Interaction of individual Ag atoms with graphene on Rh(111): Adsorption, migration, and cluster formation, Carbon **210**, 118032 (2023).

[49] M. Harb, F. Rabilloud, D. Simon, A. Rydlo, S. Lecoultre, F. Conus, V. Rodrigues, and C. Félix, Optical absorption of small silver clusters: Ag_n, $(n = 4-22)$, J. Chem. Phys. **129**, 194108 (2008).

[50] C. Yu, R. Schira, H. Brune, B. von Issendorff, F. Rabilloud, and W. Harbich, Optical properties of size selected neutral Ag clusters: electronic shell structures and the surface plasmon resonance, Nanoscale **10**, 20821 (2018).

[51] K.-P. Charlé, L. König, S. Nepijko, I. Rabin, and W. Schulze, The surface plasmon resonance of free and embedded Ag-clusters in the size range 1.5 nm < D < 30 nm, Cryst. Res. Technol. **33**, 1085 (1998).

[52] J. A. Scholl, A. L. Koh, and J. A. Dionne, Quantum plasmon resonances of individual metallic nanoparticles, Nature (London) **483**, 421 (2012).

[53] T. J. Antosiewicz, S. P. Apell, and T. Shegai, Plasmon–exciton interactions in a core–shell geometry: From enhanced absorption to strong coupling, ACS Photon. **1**, 454 (2014).

[54] C. F. Bohren and D. R. Huffman, *Absorption and Scattering of Light by Small Particles* (John Wiley & Sons, Inc., 1983).

[55] S. Tanaka, T. Yoshida, K. Watanabe, Y. Matsumoto, T. Yasuike, D. Novko, M. Petrović, and M. Kralj, Ultrafast plasmonic response ensured by atomic scale confinement, ACS Photon. **9**, 837 (2022).

[56] C. Díaz, F. Calleja, A. L. Vázquez de Parga, and F. Martín, Graphene grown on transition metal substrates: Versatile templates for organic molecules with new properties and structures, Surf. Sci. Rep. **77**, 100575 (2022).

[57] Y. Pan, M. Gao, L. Huang, F. Liu, and H.-J. Gao, Directed self-assembly of monodispersed platinum nanoclusters on graphene Moiré template, Appl. Phys. Lett. **95**, 093106 (2009).

[58] P.-Y. Cai, Y.-W. Huang, Y.-C. Huang, M.-C. Cheng, L.-W. Lan, C.-C. Kuo, J.-H. Wang, and M.-F. Luo, Atomic structures of Pt nanoclusters supported on graphene grown on Pt(111), J. Phys. Chem. C **122**, 16132 (2018).

[59] A. T. N'Diaye, S. Bleikamp, P. J. Feibelman, and T. Michely, Two-dimensional Ir cluster lattice on a graphene moiré on Ir(111), Phys. Rev. Lett. **97**, 215501 (2006).

[60] A. Cavallin, M. Pozzo, C. Africh, A. Baraldi, E. Vesselli, C. Dri, G. Comelli, R. Larciprete, P. Lacovig, S. Lizzit, and D. Alfé, Local electronic structure and density of edge and facet atoms at Rh nanoclusters self-assembled on a graphene template, ACS Nano **6**, 3034 (2012).

[61] M. Sicot, S. Bouvron, O. Zander, U. Rüdiger, Y. S. Dedkov, and M. Fonin, Nucleation and growth of nickel nanoclusters on graphene moiré on Rh(111), Appl. Phys. Lett. **96**, 093115 (2010).

[62] A. T. N'Diaye, T. Gerber, C. Busse, J. Myslivečeк, J. Coraux, and T. Michely, A versatile fabrication method for cluster superlattices, New J. Phys. **11**, 103045 (2009).

[63] E. Sutter, P. Albrecht, B. Wang, M.-L. Bocquet, L. Wu, Y. Zhu, and P. Sutter, Arrays of Ru nanoclusters with narrow size distribution templated by monolayer graphene on Ru, Surf. Sci. **605**, 1676 (2011).

[64] B. Wang and M.-L. Bocquet, Monolayer graphene and h-BN on metal substrates as versatile templates for metallic nanoclusters, J. Phys. Chem. Lett. **2**, 2341 (2011).

[65] M. Zarshenas, V. Gervilla, D. G. Sangiovanni, and K. Sarakinos, Room-temperature diffusion of metal clusters on graphene, Phys. Chem. Chem. Phys. **23**, 13087 (2021).

[66] D. V. Demidov, I. P. Prosvirin, A. M. Sorokin, and V. I. Bukhtiyarov, Model Ag/HOPG catalysts: preparation and STM/XPS study, Catal. Sci. Technol. **1**, 1432 (2011).

[67] I. Lopez-Salido, D. C. Lim, and Y. D. Kim, Ag nanoparticles on highly ordered pyrolytic graphite (HOPG) surfaces studied using STM and XPS, Surf. Sci. **588**, 6 (2005).

[68] S. Kazaoui, N. Minami, Y. Tanabe, H. J. Byrne, A. Eilmes, and P. Petelenz, Comprehensive analysis of intermolecular charge-transfer excited states in C_{60} and C_{70} films, Phys. Rev. B **58**, 7689 (1998).

[69] R. Bauernschmitt, R. Ahlrichs, F. H. Hennrich, and M. M. Kappes, Experiment versus time dependent density functional theory prediction of fullerene electronic absorption, J. Am. Chem. Soc. **120**, 5052 (1998).

[70] C. Chakravarty, H. Aksu, B. Maiti, and B. D. Dunietz, Electronic spectra of C_{60} films using screened range separated hybrid functionals, J. Phys. Chem. A **125**, 7625 (2021).

[71] M. W. Knight, N. S. King, L. Liu, H. O. Everitt, P. Nordlander, and N. J. Halas, Aluminum for plasmonics, ACS Nano **8**, 834 (2014).

[72] K. Chatterjee, S. Banerjee, and D. Chakravorty, Plasmon resonance shifts in oxide-coated silver nanoparticles, Phys. Rev. B **66**, 085421 (2002).

[73] C. Langhammer, M. Schwind, B. Kasemo, and I. Zorić, Localized surface plasmon resonances in aluminum nanodisks, Nano Lett. **8**, 1461 (2008).

[74] G. Zengin, T. Gschneidtner, R. Verre, L. Shao, T. J. Antosiewicz, K. Moth-Poulsen, M. Käll, and T. Shegai, Evaluating conditions for strong coupling between nanoparticle plasmons and organic dyes using scattering and absorption spectroscopy, J. Phys. Chem. C **120**, 20588 (2016).

[75] R. Baer and E. Rabani, Theory of resonance energy transfer involving nanocrystals: The role of high multipoles, J. Chem. Phys. **128**, 184710 (2008).

[76] R. F. Ribeiro, L. A. Martínez-Martínez, M. Du, J. Campos-Gonzalez-Angulo, and J. Yuen-Zhou, Polariton chemistry: controlling molecular dynamics with optical cavities, Chem. Sci. **9**, 6325 (2018).

[77] T. Yasuike and K. Nobusada, Open-boundary cluster model for calculation of adsorbate-surface electronic states, Phys. Rev. B **76**, 235401 (2007).

[78] E. Epifanovsky, III, A. T. B. Gilbert, X. Feng, J. Lee, Y. Mao, N. Mardirossian, P. Pokhilko, A. F. White, M. P. Coons, A. L. Dempwolff, Z. Gan, D. Hait, P. R. Horn, L. D. Jacobson, I. Kaliman, J. Kussmann, A. W. Lange, K. U. Lao, D. S. Levine, J. Liu *et al.*, Software for the frontiers of quantum chemistry: An overview of developments in the Q-Chem 5 package, J. Chem. Phys. **155**, 084801 (2021).

[79] F. Weigend and R. Ahlrichs, Balanced basis sets of split valence, triple zeta valence and quadruple zeta valence quality for H to Rn: Design and assessment of accuracy, Phys. Chem. Chem. Phys. **7**, 3297 (2005).

[80] D. Rappoport and F. Furche, Property-optimized Gaussian basis sets for molecular response calculations, J. Chem. Phys. **133**, 134105 (2010).

[81] D. Andrae, U. Häußermann, M. Dolg, H. Stoll, and H. Preuß, Energy-adjusted ab initio pseudopotentials for the second and third row transition elements, Theor. Chim. Acta **77**, 123 (1990).

[82] W. J. Hehre, R. Ditchfield, and J. A. Pople, Self-consistent molecular orbital methods. XII. further extensions of Gaussian–type basis sets for use in molecular orbital studies of organic molecules, J. Chem. Phys. **56**, 2257 (1972).

[83] P. C. Hariharan and J. A. Pople, The influence of polarization functions on molecular orbital hydrogenation energies, Theor. Chim. Acta **28**, 213 (1973).

[84] T. Clark, J. Chandrasekhar, G. W. Spitznagel, and P. V. R. Schleyer, Efficient diffuse function-augmented basis sets for anion calculations. III. the 3-21+G basis set for first-row elements, Li–F, J. Comput. Chem. **4**, 294 (1983).

[85] F. J. Garcia-Vidal, C. Ciuti, and T. W. Ebbesen, Manipulating matter by strong coupling to vacuum fields, Science **373**, eabd0336 (2021).

[86] *Handbook of Optical Constants of Solids*, edited by E. D. Palik (Academic Press, Burlington, 1997).